2002 - J - 9

ELSEVIER

Wear 253 (2002) 1156–1164

WEAR

www.elsevier.com/locate/wear

# Fracture range detection in hydro-abrasive erosion of concrete

A.W. Momber [a,*], R.S. Mohan [b], R. Kovacevic [c]

[a] *WOMA Apparatebau GmbH, P.O. Box 141820, D-47208 Duisburg, Germany*
[b] *Department of Mechanical Engineering, The University of Tulsa, Tulsa, OK, USA*
[c] *Department of Mechanical Engineering, Southern Methodist University, Dallas, TX, USA*

Received 28 November 2001; received in revised form 18 July 2002; accepted 15 August 2002

**Abstract**

The paper discusses fast Fourier transform (FFT) parameters of acoustic emission signals acquired during the hydro-abrasive erosion (HAE) of five different concrete mixtures. The FFT-peak amplitude as well as the FFT-peak frequency shows some pronounced relationships to the depth of penetration and to the fracture behavior of the investigated materials. Correlation statistics is used to separate three distinguished fracture ranges during HAE: intergranular erosion, mixed-mode fracture, and transgranular fracture. It is concluded that FFT-peak amplitude and FFT-peak frequency of the acoustic emission signals can be used for the on-line control of HAE-processes.

*Keywords:* Acoustic emission; Concrete; Erosion

## 1. Introduction

Hydro-abrasive erosion (HAE) is a newly introduced demolition method that offers some advantages over many other traditional and non-traditional cutting technologies, for example no thermal distortion, high machining versatility, low cutting force, very low vibration level, and high flexibility [1]. A hydro-abrasive jet is formed by accelerating small abrasive particles (usually garnet) through contact with a high-speed waterjet. The mixing between abrasives, water, and air takes place in a mixing chamber, and the acceleration process occurs in an acceleration focus [2]. The abrasive particles leave the focus at velocities of several hundred meters per second. A high number of abrasives generates a high frequency impingement on the material surface resulting in HAE [3].

HAE is a very promising tool for the deep trenching and drilling of rocks and concrete [1,3,4]. Moreover, HAE has a high potential in dismantling and decommissioning reinforced concrete parts of nuclear installations, such as the biological shield [1,5,6]. A steel-bar reinforced concrete member cut by HAE is shown in Fig. 1.

Although several parameter studies have been performed for multi-phase, quasi-brittle materials, such as refractory ceramics, concrete and rocks, the general mechanisms of material removal are not well understood. Specific problems are reviewed in [3,7]. There is, especially for outdoor applications and under remote-controlled conditions, a strong need to monitor the erosion process. This includes depth of penetration, cutting status (kerfing or separation), cut quality, energy situation and the detection of hidden mountings (old reinforcement, inclusions, lost mountings). It was shown by several authors that the acoustic emission technique (AE) has some capability to control certain HAE-parameters. It was also shown that AE has the capability to monitor the material removal mode in brittle materials subjected to HAE. A summary of these investigations is given in Table 1.

In this study, the capability of AE to distinguish between individual fracture types observed during HAE of different concrete mixtures is investigated. Concrete is used because it falls into the category of multi-phase quasi-brittle materials. There are only a few investigations known that deal in some detail with the HAE of concrete. Parameter studies were performed in [7,13] and is was found that the crack velocity can characterize the HAE-resistance [13]. It was further found that the material removal process depends strongly on the structural homogeneity of the material. Concrete with a low homogeneity (small rounded aggregate, large difference in matrix strength and inclusion strength, weak interfacial bond) fails through matrix removal and inclusion pull-out, whereas concrete with high homogeneity (large broken aggregate, small difference in matrix strength and inclusion strength, good interfacial bond) fails through transgranular

---

* Corresponding author. Tel.: +49-2065-304380;
fax: +49-2065-304200.
*E-mail address:* andreas.momber@woma.de (A.W. Momber).

0043-1648/02/$ – see front matter © 2002 Elsevier Science B.V. All rights reserved.
PII: S0043-1648(02)00237-5

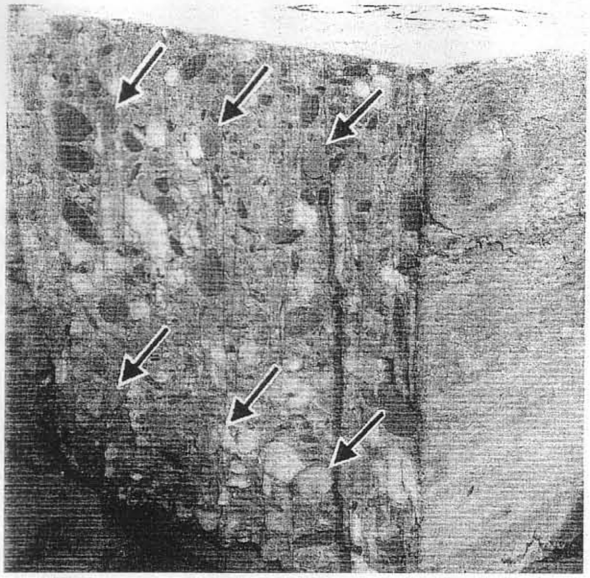

Fig. 1. Steel-bar reinforced concrete member, separated by HAE (reinforcement bars are marked: member height, 33 cm). Photograph: WOMA Apparatebau GmbH, Duisburg.

inclusion fracture [7]. In a recent study [14] it was shown that the strain energy density of concrete materials can characterize certain features of HAE, namely penetration depth, process efficiency and machinability.

## 2. Experimental set-up and procedure

### 2.1. Test materials

Five different concrete mixtures were designed and six specimens of each mixture were manufactured. The mechanical properties of these materials were influenced by changing water–cement-ratio and aggregate fineness (Table 2). Strength of the cement matrix as well as average inclusion diameter increases in the order from concretes 1 to 5. After mixing and placing, the mixtures were cured and hardened for 28 days under water. After hardening, three specimens of each mixture were tested to estimate the mechanical properties, namely compressive strength, Young's modulus, density and strain energy density. All values are listed in Table 2. The dimensions of the cylindrical specimens used for these tests were 30 cm in length and 15 cm in diameter. The compressive strength was measured according to the ASTM standard C 39, and the Young's modulus was estimated according to the ASTM standard C 469. The strain energy density was calculated by integrating the experimentally estimated stress-strain functions.

### 2.2. Experimental set-up

The experimental set-up consisted of an HAE-system, AE-sensor, pre-amplifier, ac/dc converter, AE-monitoring system, and PC/AT with suitable software. The HAE-system

Table 1
HAE-process control by acoustic emission measurements

| Material | AE-parameters | Application | Objective/results | Reference |
|---|---|---|---|---|
| Alumina ceramics | RMS, voltage | Drilling | Monitor process parameter influence<br>Detect borehole cracking | [8] |
| Aluminum | PSD (ARMA modeling)<br>Amplitude | Cutting | Control penetration depth<br>Cutting-through control | [9] |
| Cast iron | PSD (ARMA modeling) | 3-D machining | Monitor process energy absorption | [10] |
| Concrete | FFT-peak amplitude<br>RMS, voltage | Kerfing | Control macroscopic material removal<br>Control material property influence | [7] |
| Refractory ceramics | Signal amplitude<br>Signal amplitude<br>PSD (ARMA modeling) | Cutting<br>Piercing | Monitor material fracture mode<br>Monitor individual piercing stages<br>Control hole quality | [11]<br>[12] |

RMS, root mean square value; PSD, power spectrum density; ARMA, auto regressive model analysis; FFT, fast Fourier transform.

Table 2
Mechanical properties of the used materials

| Concrete mixture | Young's modulus (GPa) | Compressive strength (MPa) | Strain energy density (MJ/m$^3$) | Density (kg/m$^3$) | Water–cement[a] ratio | Coarse aggregates[b] (%) |
|---|---|---|---|---|---|---|
| 1 | 10.7 | 4.0 | 2.1 | 1962 | 0.85 | 20 |
| 2 | 24.1 | 12.5 | 11.1 | 2107 | 0.71 | 30 |
| 3 | 33.0 | 27.1 | 38.9 | 2135 | 0.45 | 40 |
| 4 | 34.3 | 34.2 | 62.6 | 2275 | 0.38 | 50 |
| 5 | 42.3 | 41.1 | 72.8 | 2343 | 0.32 | 60 |

[a] Portland cement, type I.

[b] Broken limestone (maximum grain size 19 mm).

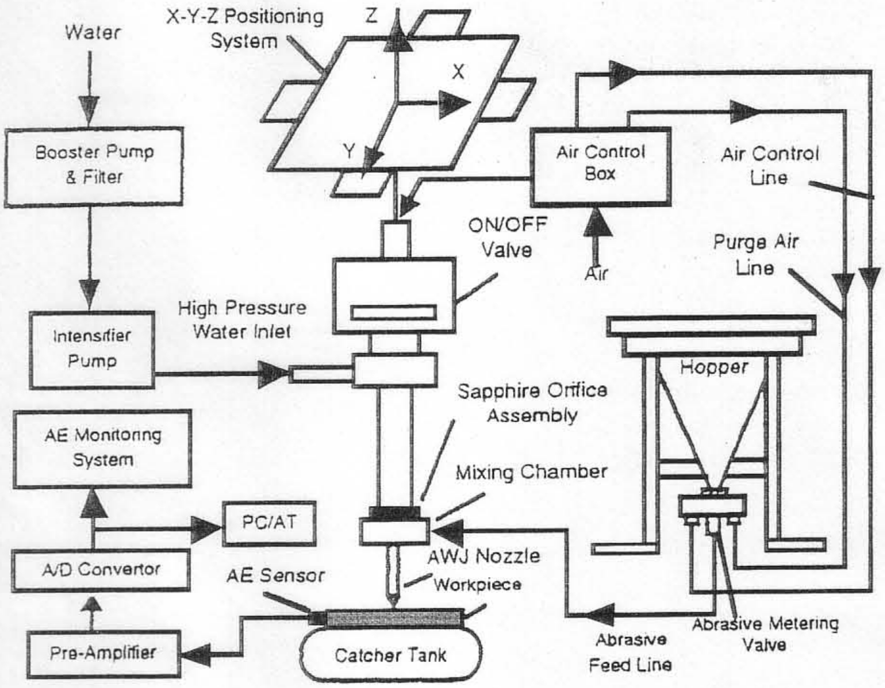

Fig. 2. Experimental set-up.

used for conducting the experiment consisted of a high-pressure intensifier pump, machining head, abrasive metering and delivery system, abrasive hopper with garnet as abrasive, catcher tank, and X–Y–Z positioning system controlled by a CNC-controller. The experimental set-up is shown in Fig. 2. Some HAE-parameters, namely abrasive velocity, local exposure time, and abrasive consumption were varied. These parameters are the most important parameters from the point of view of practical application, because they can be varied without interruption of the erosion (cutting) process. The abrasive velocity was approximated by the following equation:

$$v_{\mathrm{P}} = \frac{\alpha\varphi\sqrt{2p}}{\sqrt{\rho_{\mathrm{W}}}(1 + \dot{m}_{\mathrm{P}}/\dot{m}_{\mathrm{W}})} \quad (1)$$

The momentum transfer parameters $\alpha$ and $\varphi$ have been estimated by jet impact-force measurements (see [2,3] for further information). In Eq. (1), $p$ is the pump pressure, $\rho_{\mathrm{W}}$ the fluid density, $\dot{m}_{\mathrm{P}}$ the abrasive mass flow rate, and $\dot{m}_{\mathrm{W}}$ is the fluid mass flow rate. All estimated values are listed in Table 4. It is known from previous studies that depth of penetration increases as abrasive velocity increases [7,13]. The local exposure time was estimated as follows:

$$t_{\mathrm{E}} = \frac{d_{\mathrm{F}}}{v_{\mathrm{T}}} \quad (2)$$

In Eq. (2), $d_{\mathrm{F}}$ is the diameter of the mixing diameter, and $v_{\mathrm{T}}$ is the traverse rate of the erosion device. All estimated values are listed in Table 4. It is known from previous studies that depth of penetration increases as exposure time increases [7,13]. However, the penetration depth approximates a stable level at comparatively long exposure time. The influence of the abrasive mass flow rate on the erosion depth is discussed elsewhere [7]. Penetration depth initially increases quickly with rising abrasive mass flow rates, but shows a saturation level at higher values of abrasive mass flow rate.

Linear cuts were generated in the specimens under each experimental condition. The depth of penetration was taken as an average of five measurements for each erosion condition. The experimental conditions are listed in Tables 3 and 4.

Table 3
Fixed experimental process parameters

| Parameter | Value |
|---|---|
| Abrasive material | Garnet |
| Abrasive mesh size | #36 ($d_{\mathrm{P}} = 425\,\mu$m) |
| Abrasive particle shape | Angular (random) |
| Abrasive condition | Dry |
| Method of feed | Suction |
| Orifice material | Sapphire |
| Orifice diameter | 0.457 mm |
| Mixing nozzle length | 88.9 mm |
| Mixing nozzle diameter | 1.27 mm |
| Stand-off distance | 6.0 mm |
| Impact angle | 90° |
| Workpiece details | |
| Material | Mixtures 1–5 |
| Workpiece thickness | 310 mm |
| Length of cut | 50–80 mm |

Table 4
Variable experimental process parameters

| No. | Parameter | | | | |
|---|---|---|---|---|---|
| | Pressure (MPa) | Abrasive velocity (m/s) | Traverse rate (mm/s) | Exposure time (ms) | Abrasive mass flow rate (g/s) |
| 1 | 100 | 259 | 4.0 | 317 | 7.41 |
| 2 | 150 | 308 | 4.0 | 317 | 7.41 |
| 3 | 200 | 379 | 4.0 | 317 | 7.41 |
| 4 | 250 | 444 | 4.0 | 317 | 7.41 |
| 5 | 300 | 474 | 4.0 | 317 | 7.41 |
| 6 | 350 | 515 | 4.0 | 317 | 7.41 |
| 7 | 200 | 379 | 2.0 | 635 | 7.41 |
| 8 | 200 | 379 | 6.0 | 212 | 7.41 |
| 9 | 200 | 379 | 8.0 | 159 | 7.41 |
| 10 | 200 | 379 | 12.0 | 106 | 7.41 |
| 11 | 200 | 379 | 4.0 | 317 | 6.12 |
| 12 | 200 | 379 | 4.0 | 317 | 10.58 |
| 13 | 200 | 379 | 4.0 | 317 | 14.32 |
| 14 | 200 | 379 | 4.0 | 317 | 19.00 |

The generated AE-signals were detected and processed by a model 'AET 5500' acoustic emission monitoring system consisting of an 'AET 5500' mainframe (signal processing unit), graphics terminal (interface, data storage and display) and the accessories (sensors, pre-amplifiers, etc.). As an acoustic emission caused by an induced stress or a propagating crack occurred in the test specimen, the sensors (resonant frequency 2 MHz), fixed on top of the specimens, converted this acoustic emission wave into a voltage signal which was amplified by the pre-amplifier and sent to the mainframe (16-bit microprocessor) for post-processing. The distance between cut and sensor was between 5 and 90 mm. The sensor was glued at the samples with a water resistant epoxy-adhesive. The raw signal from the AE-monitoring system was acquired at 1 MHz sampling frequency (with a gain of 1.0 and 5.0, respectively) using a suitable PC-based data acquisition system for spectrum analysis. Each data set consisted of 1024 discrete time domain points. Five data sets of the fast Fourier transform (FFT) of the time domain signals acquired under the same experimental conditions were averaged and the representative signal was obtained for analysis. A set of 14 cuts was performed for each material type under different erosion conditions (abrasive velocity, local exposure time, abrasive consumption). Thus, a summary of 350 individual signals was analyzed. The results of these measurements are listed in Table 5.

A regression analysis was performed to analyse the relationships between the penetration depth and the FFT-parameters, namely the FFT-peak frequency and FFT-peak amplitude. The following five regression types were considered: linear, polynomial (second order), geometric, exponential, and logarithmic regression. For all types, coefficient of correlation ($R^2$) and standard deviation ($S$) were estimated. In order to obtain information about the failure mode under the certain erosion conditions, the erosion sites were inspected by optical microscopy.

## 3. Results and discussion

### 3.1. FFT-peak amplitude analysis

The relationship between depth of penetration and FFT-peak amplitude is shown in Fig. 3. The following three features can be noted. Firstly, a general relationship exists between the two parameters; if depth of penetration increases, FFT-peak amplitude tends to increase. Secondly, there is a range of extraordinarily high amplitudes (marked as 'Range I'). Thirdly, there is an area of amplitude accumulation in a very narrow depth and amplitude range (marked as 'Range II').

The general trend confirms results in [9] where the same relationship for HAE of aluminium was found. However, this trend is only valid if the material is removed by a

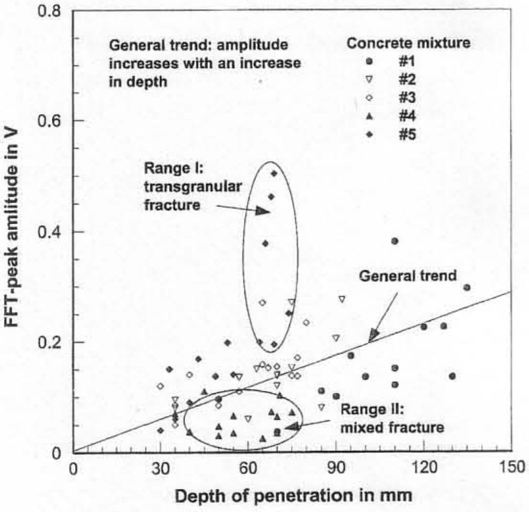

Fig. 3. Relationship between depth of penetration and FFT-peak amplitude.

Table 5
FFT-peak parameters of the AE-signals

| No. | Concrete 1 | | Concrete 2 | | Concrete 3 | | Concrete 4 | | Concrete 5 | |
|---|---|---|---|---|---|---|---|---|---|---|
| | Frequency (kHz) | Amplitude (V) | Frequency (kHz) | Amplitude (V) | Frequency (kHz) | Amplitude (V) | Frequency (kHz) | Amplitude (V) | Frequency (kHz) | Amplitude (V) |
| 1 | 142.6 | 0.0959 | 109.4 | 0.0864 | 129.9 | 0.0490 | 274.4 | 0.0703 | 127.0 | 0.1495 |
| 2 | 150.4 | 0.1115 | 131.8 | 0.1585 | 105.5 | 0.0855 | 176.8 | 0.1094 | 149.4 | 0.1682 |
| 3 | 138.7 | 0.1531 | 139.7 | 0.1441 | 142.6 | 0.1523 | 159.2 | 0.0656 | 142.6 | 0.1969 |
| 4 | 147.5 | 0.2240 | 134.8 | 0.1521 | 144.5 | 0.1328 | 167.0 | 0.0734 | 147.5 | 0.3771 |
| 5 | 138.7 | 0.2250 | 105.5 | 0.2043 | 140.6 | 0.1367 | 165.0 | 0.0641 | 138.7 | 0.4609 |
| 6 | 117.2 | 0.2951 | 119.1 | 0.2755 | 127.0 | 0.2330 | 152.3 | 0.1031 | 161.1 | 0.5031 |
| 7 | 156.3 | 0.3805 | 120.1 | 0.1192 | 158.2 | 0.2734 | 194.3 | 0.0347 | 169.0 | 0.1414 |
| 8 | 159.2 | 0.1104 | 160.2 | 0.1356 | 149.4 | 0.1400 | 208.0 | 0.0470 | 131.8 | 0.0891 |
| 9 | – | – | – | – | 129.9 | 0.0864 | 142.6 | 0.0370 | 166.0 | 0.0566 |
| 10 | 115.2 | 0.0371 | 126.0 | 0.0951 | 162.1 | 0.1242 | – | – | 146.5 | 0.0406 |
| 11 | 137.7 | 0.1734 | 127.9 | 0.0631 | 137.7 | 0.1095 | 180.7 | 0.0312 | 123.1 | 0.1367 |
| 12 | 164.6 | 0.1354 | 102.5 | 0.1372 | 130.9 | 0.1578 | 193.4 | 0.0250 | 143.6 | 0.1982 |
| 13 | 113.3 | 0.1203 | 125.0 | 0.2724 | 100.6 | 0.1543 | 132.8 | 0.0352 | 109.4 | 0.1941 |
| 14 | 108.4 | 0.1354 | 128.9 | 0.0775 | 117.2 | 0.1697 | 213.9 | 0.0722 | 148.4 | 0.2520 |

particular failure mode. If only one particular material removal mode contributes to the material failure, the following statement can be made. The more material is removed the more individual events occur that produce AE-signals. As far as the failure mode changes or a mixed-mode failure occurs, the correlation drops because the mode of failure influences the energy level of the generated AE-signal. Therefore, for a given depth of penetration, the stronger material usually exhibits the higher peak amplitude. This is in particular true for the concrete 5.

Range I in Fig. 3 characterizes a process that generates very high values of AE-signal energy. Interestingly, most of these points belong to concrete 5. For a given depth of penetration, concrete 5 produces unusually high FFT-peak amplitudes. Optical microscopy photographs showed that this material entirely fails in a transgranular fashion with fracture planes running through the aggregate inclusions. Many of such broken aggregate grains (large limestone grains as well as small quartz particles) can be seen in Fig. 6a. It was shown in a previous study [7] that this erosion type produces burst-type AE-signals with a sudden release of high-energy stresses caused by the forced fracture of the aggregate particles. This explanation holds also for the extraordinarily high peak amplitudes in Fig. 3.

In the Range II, marked in Fig. 3, the FFT-peak amplitudes show unusual tendencies. Firstly, the amplitudes are very low. Secondly, the amplitude values are concentrated in a narrow amplitude range under the base line. There is no certain trend between peak amplitude and depth of penetration in that range. This range contains mostly signals from the concrete 4. For a given depth of penetration, this concrete mixture produces comparatively low FFT-peak amplitudes. The microscopic inspection of the erosion site showed that this material fails through a mixture of intergranular erosion and transgranular fracture. The first fracture mode (intergranular erosion) is characterized by the removal of the weak cement matrix and the subsequent pull-out of the individual aggregates. Characteristic features are exposed, but undamaged, inclusions and circular cavities in the matrix as shown in Fig. 6b. However, this mode dominates the removal process. The second fracture mode (transgranular fracture) is characterized by forced fracture of the aggregates; this is illustrated in the upper central region of Fig. 6b. This transition between intergranular fracture and transgranular fracture is accompanied by certain energy absorbing processes, such as crack deflection, crack arrest, crack branching and microcrack shielding [15]. Especially the latter two processes could reduce the energy of individual AE-signals. This could be the reason for the large difference in the FFT-amplitudes of concretes 4 and 5 in the range of almost equal penetration depths (between 65 and 70 mm). The energy absorbing processes may also explain the higher FFT-amplitudes for concretes 2 and 3 compared to those of concrete 4. In the low-strength mixtures the removal of the weak matrix and the corresponding pull-out of the exposed inclusions is the only material removal mode (compare Fig. 6c); it is not accompanied by crack branching and crack arrest. Controlled crack grow occurs along the interface between matrix and inclusion.

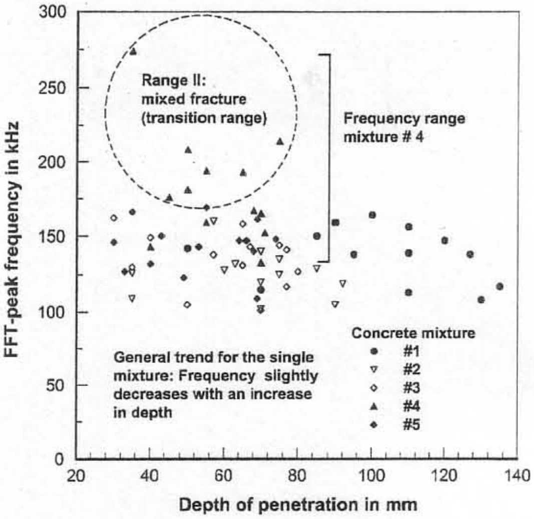

Fig. 4. Relationship between depth of penetration and FFT-peak frequency.

## 3.2. FFT-peak frequency analysis

Fig. 4 shows the relationship between the depth of penetration and the FFT-peak frequency of the signals. Again, three distinguished features can be noticed. Firstly, there is a stable band of frequencies between $f_{\mathrm{FFT}} = 100\,\mathrm{kHz}$ and $f_{\mathrm{FFT}} = 175\,\mathrm{kHz}$ over the entire depth-of-penetration range. This band contains 90% of all signals. Inside this band, for a particular material, the FFT-peak frequency slightly reduces with an increase in the penetration depth. Secondly,

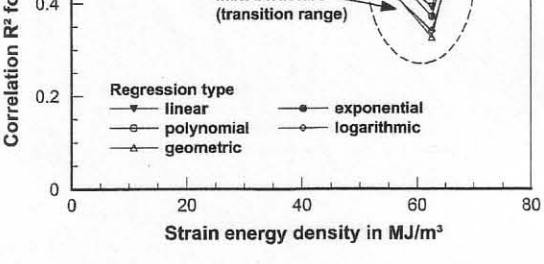

Fig. 5. Regression correlations for FFT-peak amplitude vs. depth of penetration.

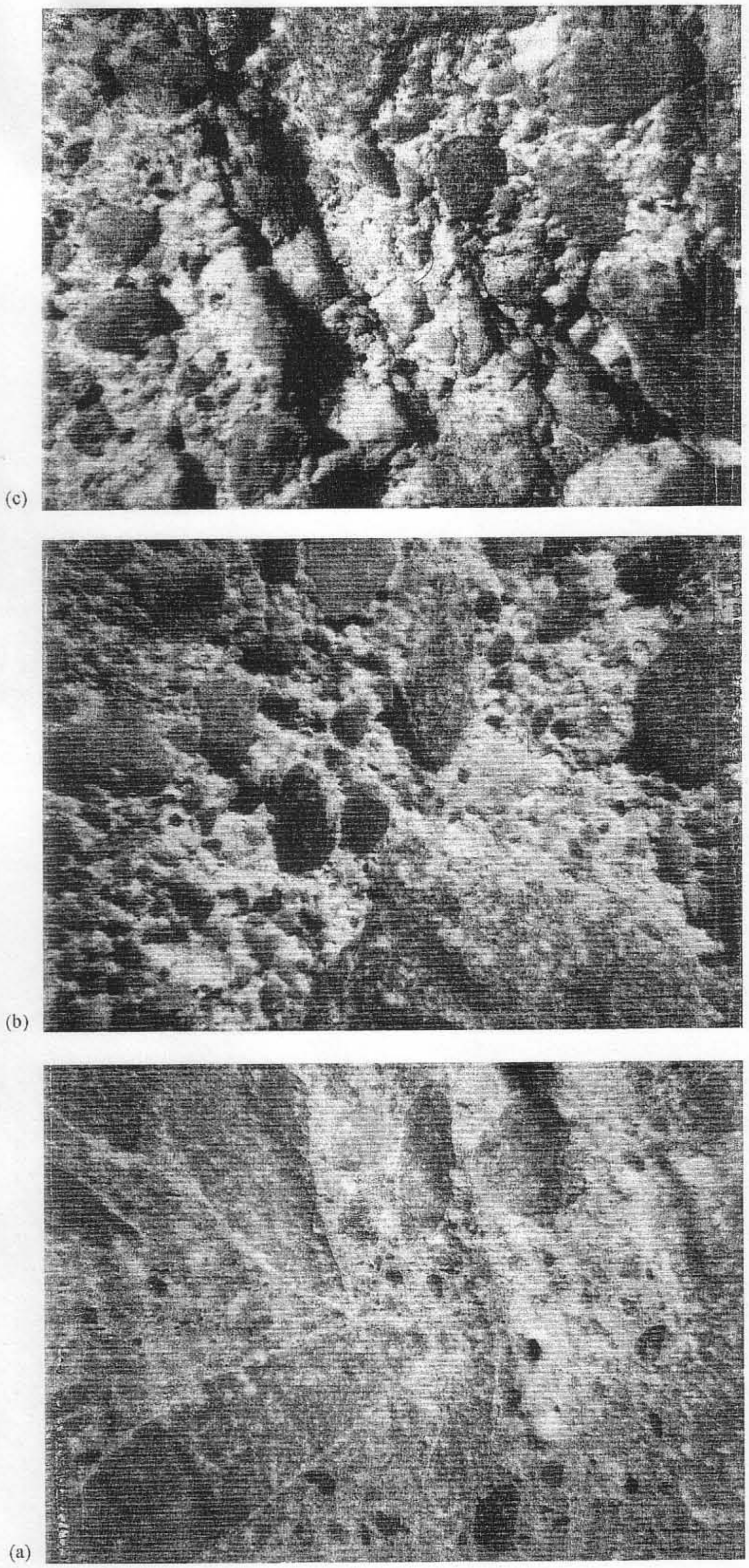

Fig. 6. Optical microscope photographs from erosion sites: (a) transgranular fracture, magnification 30× (concrete 5); (b) mixed-mode failure, magnification 50× (concrete 4); (c) intergranular erosion, magnification 50× (concrete 1).

there exists a range of unusually high frequencies (marked as 'Range II'). Thirdly, one of the materials (mixture 4) covers an extraordinarily wide frequency range.

The signals inside the small band belong to the mixtures 1–3 and to the mixture 5 which are the materials that are eroded by single-mode fracture. Although both single-mode fracture types are quite different (it can be seen from Fig. 6c that the concrete 1 fails in a completely intergranular mode) and generate different FFT-peak amplitudes (Fig. 3), their AE-signals are located in a limited frequency range.

In contrast, the concrete 4 covers a wide range of frequencies between $f_{\mathrm{FFT}} = 125\,\mathrm{kHz}$ and $f_{\mathrm{FFT}} = 275\,\mathrm{kHz}$. Moreover, this material is the only one producing frequencies higher than $f_{\mathrm{FFT}} = 175\,\mathrm{kHz}$. For a given depth of penetration, this material produces very high frequencies. From the discussion in Section 3.1 can be concluded that this high frequency range characterizes the mixed-mode failure regime in the material. It seems that FFT-peak amplitude clearly distinguishes between a single-mode failure (low values, small frequency band) and a mixed-mode failure (high values, widely spread frequencies). However, as far as a single-mode failure is identified a further subdivision is not possible, and it is not possible to link the FFT-peak frequency to the penetration depth. The signals in Range II contain information about fracture features that are neither observed during intergranular erosion (Fig. 6c) nor during transgranular fracture (Fig. 6a). Some of these features are crack deflection at the aggregate-matrix interface, crack arrest by an aggregate, or microcrack formation [15]. It seems that the formation of a microcrack net in front of a growing main crack is responsible for the high frequency of the AE-signals acquired from concrete 4. A fracture model that uses a microcrack-band to describe the failure of concrete is available in the reference literature [16].

### 3.3. Coefficient of correlation

The correlation between depth of penetration and FFT-peak amplitude is shown in Fig. 5. The coefficients of correlation for the different regression types are plotted against the five material types characterized by their strain energy density (any of the material properties listed in Table 2 would have generated the same qualitative trend). The values for the strain energy density are in the order of the material number. The five regressions are performed for each material separately. Three different ranges can be distinguished in Fig. 5. Firstly, there is a range with a high correlation (marked as 'Range I'). Secondly, there is a range with a medium correlation (marked as 'Range II'). Thirdly, a range with a low correlation can be seen (marked as 'Range III').

The Range I contains only the signals acquired from mixture 5 having the highest values of the mechanical properties. This mixture also shows the highest structural homogeneity (large aggregates, high-strength cement matrix, good matrix-aggregate bond) and a high stiffness. In the compression test, this concrete failed very brittle; the failure occurred very sudden and a high level of noise was noticed. The generated debris were large and irregular. They also showed features of almost unrestrained brittle fracture, such as broken aggregates and a smooth fracture surface [17]. This certain behavior could also be observed during the HAE of that material. As shown in Fig. 6a, the material is removed by transgranular fracture with broken inclusions and smooth fracture planes.

Similar is the situation with the materials in Range II. The mixtures included in that range (mixtures 1, 2 and 3) failed in a comparatively uniform erosion mode. As shown in Fig. 6a, this mode features exposed inclusions as well as selective matrix removal. Although this mode is completely different from that of concrete 5, it focuses on an individual predominant failure type. Moreover, the correlation for the linear regression is on an equal level for these three materials.

In the Range III the penetration depth exhibits a low correlation to the peak amplitude. This range is covered by the concrete 4. As already stated, this material is eroded by a mixed failure mode accompanied by energy dissipative processes. Whereas transgranular fracture could be observed, intergranular erosion and grain pull-out also occurred. Fig. 6b illustrates this mixed-mode behavior. In that case, different types of signals are sent to the AE-system which are, due to the different sources of occurrence, distributed over a comparatively wide frequency range (see Fig. 4). The AE-system properly reflects this difference in the individual signal frequencies. It is for this reason that the correlation is low for all regression types.

## 4. Summary and conclusions

FFT-parameters of AE-signals acquired during HAE of five different concrete mixtures are used to distinguish and control the erosion modes. The following conclusions can be drawn.

- There is a weak general trend between the depth of penetration and the FFT-peak amplitude.
- The trend improves for single-mode erosion and deteriorates for mixed-mode erosion.
- FFT-peak amplitude can be recommended for on-line control of the penetration depth in concrete materials with high homogeneity and high stiffness.
- FFT-peak frequency can be used to distinguish between single-mode erosion and mixed-mode erosion. However, FFT-peak frequency is not able to distinguish between individual types of single-mode erosion (such as between transgranular fracture and intergranular erosion).
- FFT-peak frequency can be recommended for on-line sensing unusual conditions in a concrete structure (such as crack deflection or branching by reinforcement bars, lost mountings or aggregate agglomerations).

- Further investigation are required to refine the relationships found in this study.

## Acknowledgements

The first author thanks the German Research Association (DFG), Bonn, the Alexander-von-Humboldt Foundation, Bonn, and WOMA Apparatebau GmbH, Duisburg, Germany, for financial and administrative support.

## References

[1] A.W. Momber, Water Jet Applications in Construction Engineering, Balkema, Rotterdam, 1998.

[2] A.W. Momber, Energy transfer during the mixing of air and solid particles into a high-speed water jet, Exp. Thermal Fluid Sci. 25 (2001) 131–141.

[3] A.W. Momber, R. Kovacevic, Principles of Abrasive Water Jet Machining, Springer, London, 1998.

[4] D.A. Sumers, Waterjetting Technology, E&FN Spon, London, 1995.

[5] M. Yokota, H. Nakamura, T. Konno, H. Yoshida, Y. Miura, Dismantling technique for reactor biological shield—abrasive waterjet, in: E.K. Lauritzen (Ed.), Demolition and Reuse of Concrete, E&FN Spon, London, 1994, pp. 197–206.

[6] C. Lorin, R. Rouviere, G. Pilot, Adaptation of high pressure water jets and abrasives to dismantle nuclear installation, in: K. Pflugrad, et al. (Eds.), Decommissioning of Nuclear Installations, Elsevier, London, pp. 264–278.

[7] A.W. Momber, R.S. Mohan, R. Kovacevic, On-line analysis of hydro-abrasive erosion of pre-cracked materials by acoustic emission, Theoret. Appl. Fracture Mech. 31 (1999) 1–17.

[8] G.S. Choi, G.H. Choi, Process analysis and monitoring in abrasive water jet machining of alumina ceramics, Int. J. Machine Tools Manuf. 37 (1997) 295–307.

[9] R.S. Mohan, A.W. Momber, R. Kovacevic, On-line monitoring of depth of AWJ penetration using acoustic emission technique, in: N.S. Allan (Ed.), Jet Cutting Technology, Mechanical Engineering Publication, London, 1994, pp. 649–664.

[10] R.S. Mohan, A.W. Momber, R. Kovacevic, Energy dissipation control in hydro-abrasive machining using quantitative acoustic emission, Int. J. Adv. Manuf. Syst., 2002, in press.

[11] A.W. Momber, R.S. Mohan, R. Kovacevic, An acoustic emission study of cutting bauxite refractory ceramics by abrasive water jets, J. Mater. Eng. Perform. 8 (1999) 450–454.

[12] R. Kovacevic, H.S. Kwak, R.S. Mohan, Acoustic emission sensing as a tool for understanding the mechanisms of abrasive water jet drilling of difficult-to-machine materials, Inst. Mech. Eng., J. Eng. Manuf. 212 (1998) 45–58.

[13] A.W. Momber, R. Kovacevic, Test parameter analysis in abrasive water jet cutting of rocklike materials, Int. J. Rock Mech. Min. Sci. 34 (1997) 17–25.

[14] A.W. Momber, Stress-strain relation for water-driven particle erosion of quasi-brittle materials, Theoret. Appl. Fracture Mech. 35 (2001) 19–37.

[15] S.H. Shah, C. Ouyang, Toughening mechanisms in quasi-brittle materials, ASME J. Eng. Mater. Technol. 115 (1993) 300.

[16] Z. Bazant, B.H. Oh, Crack band theory for fracture of concrete, Mater. Struct. 16 (1983) 155–177.

[17] A.W. Momber, The fragmentation of standard concrete cylinders under compression, Eng. Fracture Mech. 67 (2000) 445–459.